Lithographically patterned nanowire electrodeposition

E. J. MENKE, M. A. THOMPSON*, C. XIANG*, L. C. YANG AND R. M. PENNER†

Institute For Surface and Interface Science and Department of Chemistry, University of California, Irvine, California 92679-2025, USA

*These authors contributed equally to this work

†e-mail: rmpenner@uci.edu

Published online: 22 October 2006; doi:10.1038/nmat1759

Nanowire fabrication methods can be classified either as 'top down', involving photo- or electron-beam lithography, or 'bottom up', involving the synthesis of nanowires from molecular precursors. Lithographically patterned nanowire electrodeposition (LPNE) combines attributes of photolithography with the versatility of bottom-up electrochemical synthesis. Photolithography defines the position of a sacrificial nickel nanoband electrode, which is recessed into a horizontal trench. This trench acts as a 'nanoform' to define the thickness of an incipient nanowire during its electrodeposition. The electrodeposition duration determines the width of the nanowire. Removal of the photoresist and nickel exposes a polycrystalline nanowire—composed of gold, platinum or palladium—characterized by thickness and width that can be independently controlled down to 18 and 40 nm, respectively. Metal nanowires prepared by LPNE may have applications in chemical sensing and optical signal processing, and as interconnects in nanoelectronic devices.

Electron-beam lithography (EBL), invented in the early 1970s[1,2], provides a means for patterning polycrystalline metal nanowires as small as 20 nm in diameter onto surfaces[3]. The applicability of EBL, however, has been limited to research and development applications, because it is a serial patterning technology. In 1990, a parallel version of EBL was described[4,5], but space-charge 'blurring'[6] has prevented this technique from approaching the resolution of direct-write EBL. By using, as a template, semiconductor surfaces with atomically defined grooves and troughs, sub-10 nm metal nanowires have been prepared using vapour deposition[7–9]. A variant of this approach was used to create high-density arrays of linear, 10-nm-diameter Pt nanowires[10]. We have demonstrated[11] that ensembles of 30 nm antimony nanowires can be prepared by electrochemical step-edge decoration on graphite surfaces coupled with etching, but no control of nanowire position on the surface or inter-wire pitch is possible using this method.

Lithographically patterned nanowire electrodeposition (LPNE) is a new method for synthesizing noble-metal nanowires on glass or oxidized silicon surfaces. LPNE (Fig. 1) involves the preparation of a sacrificial nickel nanoband electrode using optical lithography and the subsequent electrodeposition of a noble-metal (Au, Pt or Pd) nanowire at this electrode. However there is an important wrinkle: the nickel nanoband electrode is recessed into a horizontal trench defined by the insulator surface and photoresist. The electrodeposition of a nanowire into this 'nanoform' produces a wire with a rectangular cross-section, where the thickness and width are independently controllable with ≈5 nm precision, down to 18 nm in height and 40 nm in width. Because we use optical lithography to define the position of the nanowires on the surface, the optical diffraction limit constrains the spacing between nanowires.

The position of nickel nanoband electrodes prepared in the first four steps of the LPNE process shown in Fig. 1 determines the position of nanowires on a glass surface. Fritsch and co-workers[12] prepared gold nanoband electrodes using essentially the same first four steps as shown here, but our method departs in an important way from that of Fritsch in step 4: we remove exposed nickel electrochemically by applying an oxidizing potential in the range from −0.085 to −0.10 V versus a saturated calomel reference

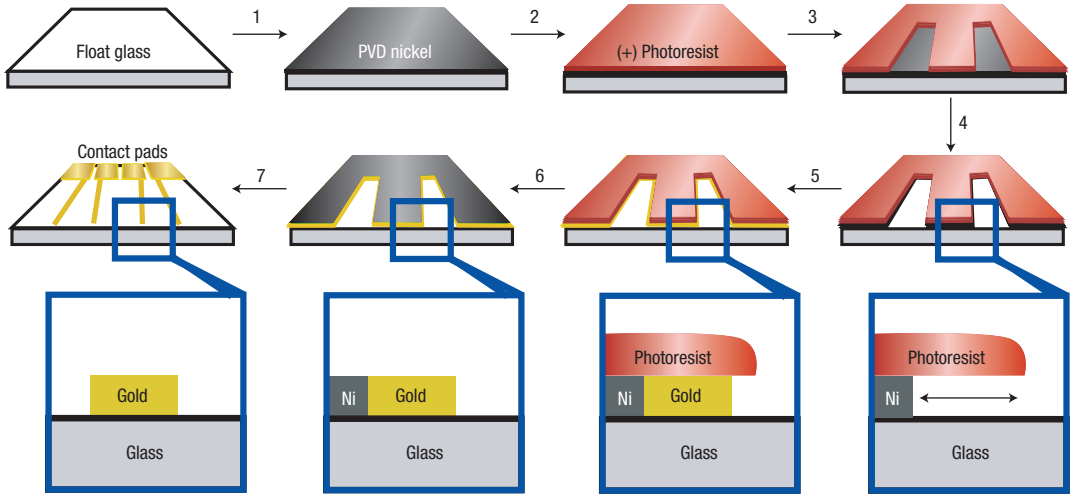

Figure 1 Seven-step process flow for metal-nanowire fabrication using LPNE.

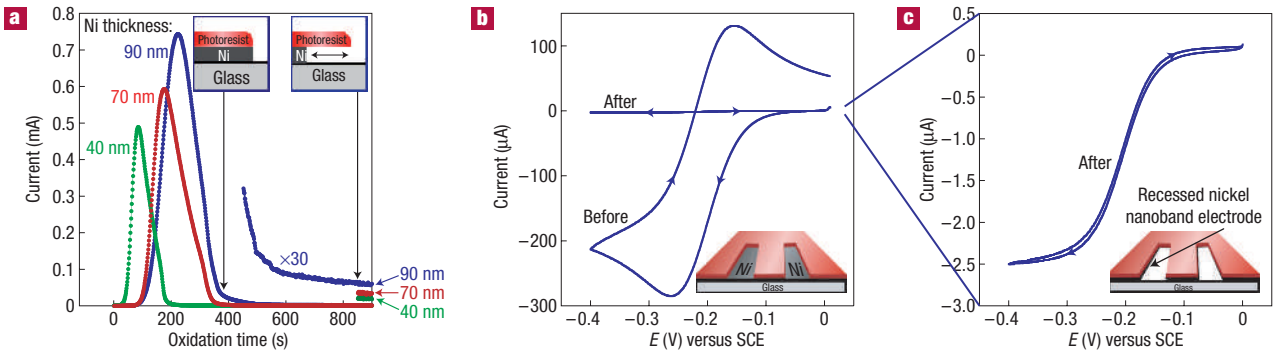

Figure 2 'Overetching' of the nickel layer produces a horizontal trench originating at the edge of the photoresist. a, Oxidation current versus time during the removal of nickel from lithographically patterned surfaces by potentiostatic electro-oxidation (reaction: $Ni \rightarrow Ni^{2+} + 2e^-$) at −0.10 V versus SCE in aqueous 0.1 M KCl at pH = 1.0. Three transients are shown for nickel layers with approximate thicknesses of 40, 70 and 90 nm, as shown. **b**,**c**, Cyclic voltammogram for $Ru(NH_3)_6^{3+}$ at 5 mV s^{-1} in aqueous 0.1 M NaCl before the removal of nickel (**b**) and after the removal of nickel (**c**) by electro-oxidation, resulting in the formation of a horizontal trench ≈200 nm in depth, terminated by a nickel nanoband 40 nm in thickness.

electrode (SCE) (Fig. 2a). We continue nickel oxidation until we etch nickel at the exposed edges of this pattern, undercutting the photoresist by 100–300 nm (Fig. 2a). For nickel films of three thicknesses (Fig. 2a), the etching current is approximately proportional to the nickel film thickness as this electrochemical undercutting occurs. Nickel 'overetching' produces a horizontal trench into which we electrodeposit a noble-metal nanowire in step 5 (Fig. 1).

Is this recessed nickel nanoband both electrochemically reactive and accessible to redox species? To answer this question, we investigated the cyclic voltammetry of $Ru(NH_3)_6^{3+}$, a metal complex that undergoes a fast, reversible one-electron reduction. Before nickel dissolution (Fig. 2b), the cyclic voltammogram shows current peaks and hysteresis of the forward and reverse scans: all consistent with the planar diffusion of this molecule to the relatively large nickel areas exposed by the dissolution of photoresist after lithography. After electro-oxidation of the nickel and the formation of the horizontal trench (Fig. 2c), the $Ru(NH_3)_6^{3+}$ reduction current was reduced by a factor of more than 100 and a steady-state, sigmoidal CV showing no hysteresis was observed, qualitatively as expected for a nanoband electrode[13]. This result demonstrates that the recessed nickel electrode is both electrochemically active and accessible to the dissolved redox species $Ru(NH_3)_6^{3+}$, as required for nanowire electrodeposition.

The growth of this nanowire into this horizontal trench occurs in three phases (Fig. 3): First, immediately after the application of a plating voltage for palladium, the current increases as palladium nucleates along the entire length of the nickel nanoband. When this nucleation process is complete, we observe a quasi-constant deposition current during growth of the confined metal nanowire because the wetted surface area of the confined wire is constant, and because for such a kinetically controlled reaction the deposition current per unit area of the metal is constant[13]. Terminating growth during this phase results in a nanowire having a rectangular cross section, such as seen in Fig. 3b. If we continue wire growth, deposited metal fills the trench and begins to emerge from it, and the total current increases because the wetted surface area increases. This 'blooming' of the nanowire as it emerges from the trench is undesirable, because it produces a distribution of dendrites along one edge of the nanowire (Fig. 3c).

The nanowires produced by LPNE have an approximately rectangular cross-section (Fig. 5a), which is enforced by the dimensions of the horizontal trench. The minimum dimensions for the thickness and width of these nanowires are 18 and 40 nm, respectively. For example, we show a platinum nanowire with a thickness of 39 nm, a width of 46 nm and a length of 1 cm in the SEM image of Fig. 4a. We can lithographically pattern large substrate areas exceeding 1 cm^2 with nanowires (for example Fig. 4b–d). The nanowires produced show remarkable dimensional uniformity over the entire sample surface. The relative standard deviations of the nanowire thickness and width are <5% and 10–12%, respectively, for the patterns shown in Fig. 4. We take particular note of the fact that corners, such as those present in the pattern of Fig. 4c, do not cause either narrowing or thickening of the nanowire—the latter expected for a diffusion-controlled deposition process. We expect this curvature invariance of the wire width if the wire electrodeposition reaction occurs under conditions of kinetic, not diffusion, control.

We can independently control the thickness and width of these nanowires: the nickel layer thickness fixes the thickness of the nanowires, whereas the width is proportional to the electrodeposition duration. We document this control by the data shown in Fig. 5b,c. The AFM-measured nanowire thickness increases linearly with the nickel layer thickness for nanowires composed of gold, palladium and platinum (Fig. 5b). The slope of these data points is 0.98, indicating that the nanowire thickness is equal to the thickness of the evaporated nickel layer. The smallest attainable nanowire thicknesses were in the 18 nm range for Au and Pt and somewhat larger for Pd. Nanowire thicknesses for all three metals in the 15 nm range will probably be possible with some additional refinement of the nickel evaporation conditions to further improve the uniformity of this film. For a metal-electrodeposition process occurring within a rectangular trench at a time-invariant current density J_{dep}, the width of the deposited nanowire, w, is given by

$$w(t) = \frac{J_{dep} t_{dep} V_m}{nF}, \qquad (1)$$

where t_{dep} is the deposition time, V_m is the molar volume of the deposited metal, n is the number of electrons required to reduce each metal complex ion and F is the Faraday constant (96,485 C $eq.^{-1}$). Plots of w versus t_{dep} for gold, palladium and platinum (Fig. 5c) are all approximately linear in accordance with equation (1). The slopes of these plots are proportional to J_{dep}, the magnitude of which depends on the concentration of metal complex present in the plating solution and on the electrodeposition potential. We have not yet established how J_{dep} influences the width uniformity of LPNE nanowires. Based on our prior work[14], there are good reasons to believe that a slower deposition rate may reduce the wire width variability, making possible the preparation of nanowires that are narrower than the minimum of 40 nm demonstrated here.

Previous measurements of the electrical properties of metal nanowires have used wires ranging in length from 500 nm (refs 15,16) to 5 μm (refs 16–18). Using a four-point probe shown in Fig. 6a (inset), we measured the electrical behaviour of 400 μm long sections of two gold nanowires with cross-sections of 20 nm × 233 nm and 100 nm × 166 nm. Two characteristics of metallic conduction are seen in these nanowires: first, the current–voltage behaviour was ohmic (Fig. 6a), and second, we observed a positive temperature coefficient of resistivity, α (Fig. 6b). However, we also see clear quantitative differences in the behaviour of these nanowires associated with their diminutive size. The measured room-temperature electrical resistivity of these nanowires was

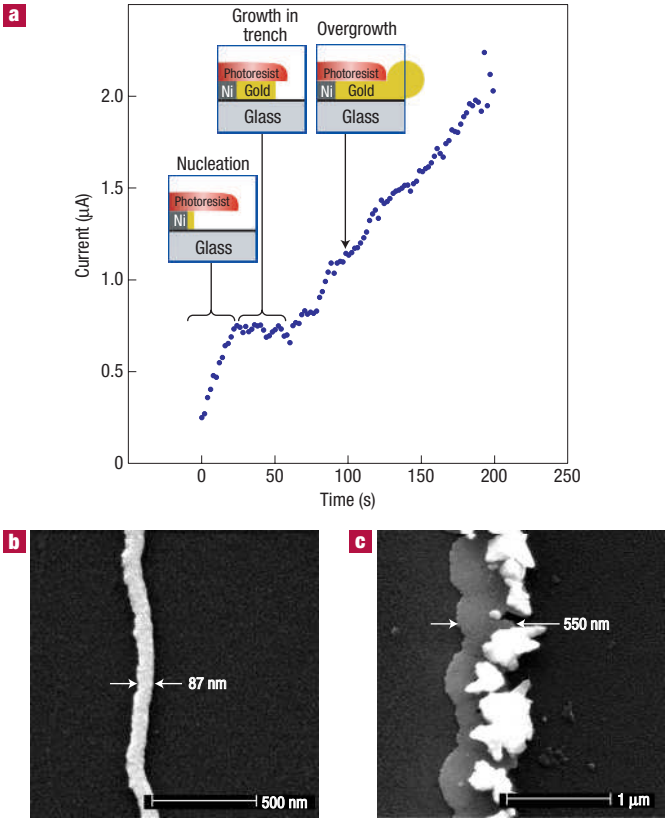

Figure 3 The filling and the eventual overfilling of the trench with gold, platinum or palladium produces a distinctive wire electrodeposition-current transient. a, Electrodeposition current versus time for the potentiostatic growth, and overgrowth, of a palladium nanowire at +0.225 V versus SCE. This aqueous solution contained 2 mM $PdCl_2$, 2 mM saccharin and 0.1 M KCl. We observe the quasi-constant current seen from 20 to 50 s because, for this kinetically controlled deposition process, current is proportional to the wetted surface area, which remains constant while growth of the nanowire is confined to the horizontal trench. **b**, Gold nanowire with a rectangular cross-section obtained for trench-confined growth for 100 s. **c**, Gold nanowire deposited for 1,000 s, showing 'blooming' from the edge of the photoresist.

significantly higher than expected for bulk gold (Table 1), and this disparity increased with decreasing temperature, down to 10 K (Fig. 6a), just as reported for nanowires in several previous studies[15–19]. How can these disparities be understood?

Two factors contribute to the resistivity of polycrystalline nanowires: (1) inelastic scattering of conduction electrons at wire surfaces[20,21] and (2) the reflection of electrons at grain boundaries[22]. Steinhogl *et al.*[23] calculated the extra resistivity contributed by these two mechanisms for nanowires with a rectangular cross-section. Their equation (our equation (2)) uses Fuchs–Sondheimer theory[20,21] to account for surface scattering and Mayadas and Shatzkes theory[22] to account for grain-boundary scattering[23]:

$$\rho = \rho_0 \left\{ \frac{1}{3} \Big/ \left[\frac{1}{3} - \frac{\alpha}{2} + \alpha^2 - \alpha^3 \ln\left(1 + \frac{1}{\alpha}\right) \right] + \frac{3}{8} C(1-p) \frac{1+AR}{AR} \frac{\lambda}{w} \right\} \quad \text{with } \alpha = \frac{\lambda}{d} \frac{R}{1-R}, \qquad (2)$$

where AR is the ratio of wire height to wire width and C is a geometrical parameter, which is equal to 1.2 for nanowires with

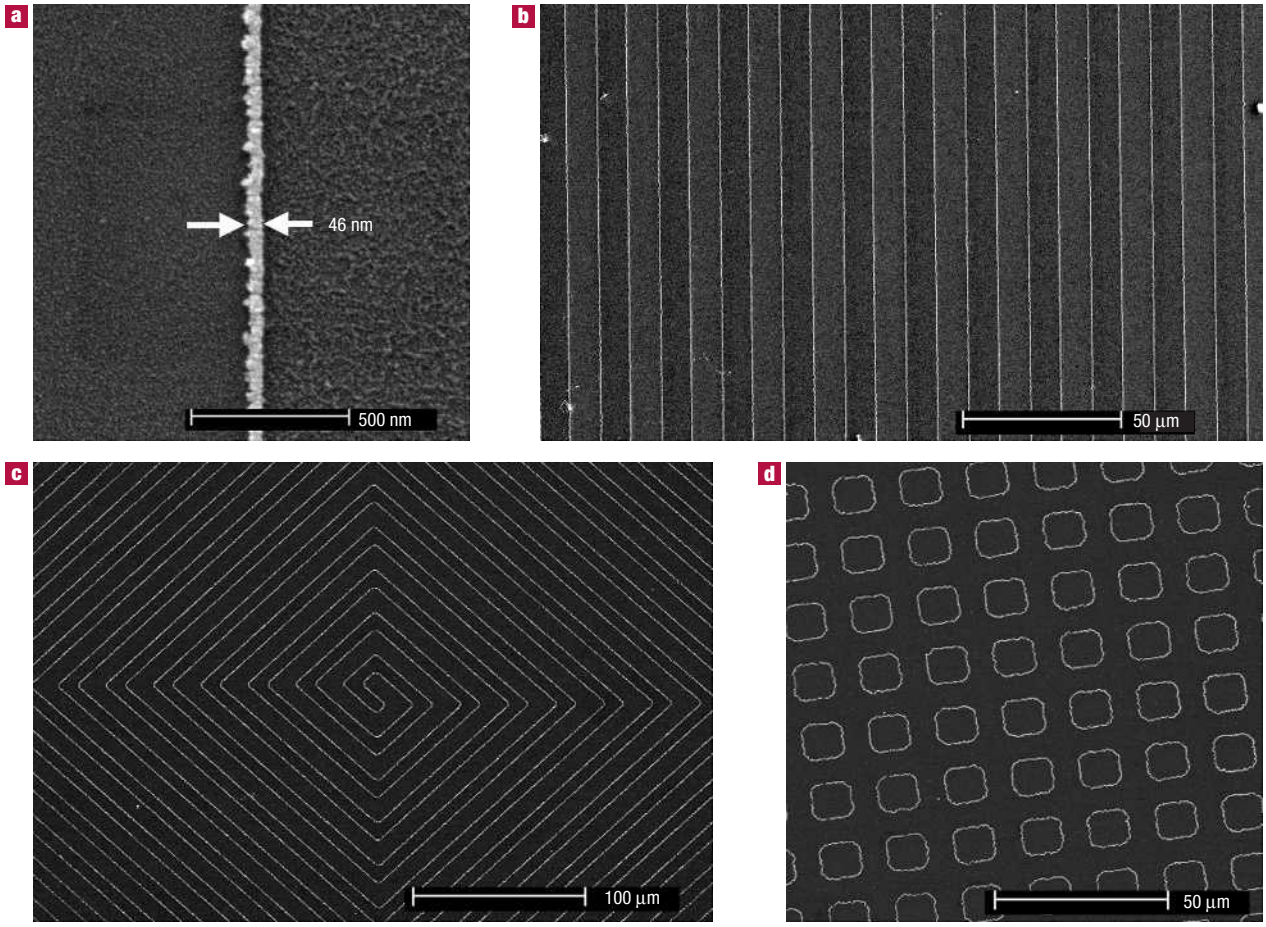

Figure 4 Examples of patterned nanowires prepared using LPNE. a, A platinum nanowire with a width of 46 nm and a thickness of 39 nm. This nanowire was continuous, as measured by scanning electron microscopy (SEM), for more than 1 cm. **b**, Parallel gold nanowires, 1 cm in length and spaced by 9 μm. **c**, A coiled nanowire with a total length of 2.7 cm. **d**, Nanowire loops.

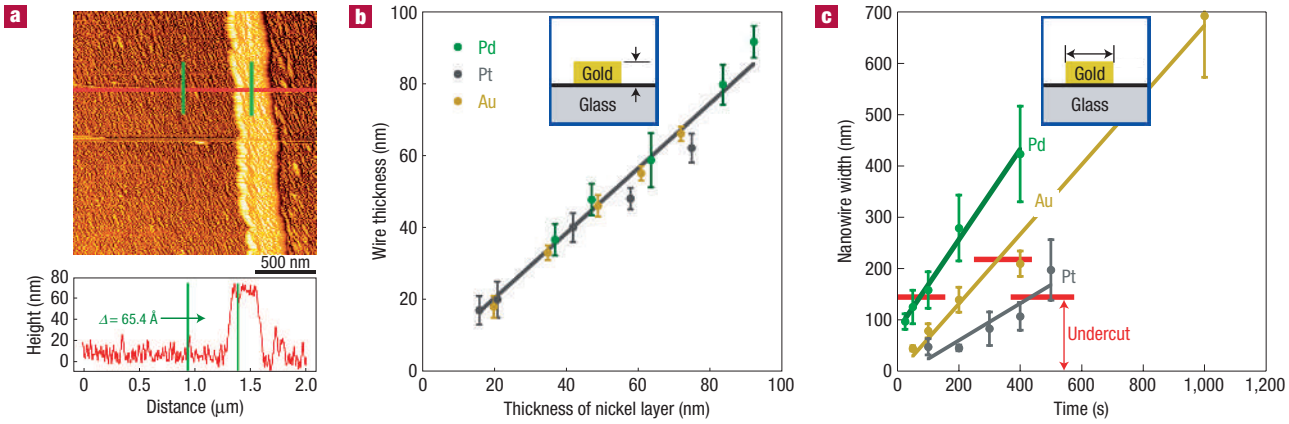

Figure 5 Both the thickness of a nanowire produced by LPNE and its width may be independently controlled. a, Atomic force microscope (AFM) image of a gold nanowire prepared using the LPNE method on glass, with the flat wire profile shown below. **b**, Nanowire thickness, measured by AFM, versus the thickness of the nickel layer deposited in step 1. **c**, Nanowire width, measured by SEM, as a function of the electrodeposition time. For both **b** and **c**, error bars represent $\pm 1\sigma$ for at least ten measurements of each nanowire.

a rectangular cross-section. w is the width of the nanowire and d is the mean grain size, which is in the 10–20 nm range. We assume other parameters specific to gold to be as follows: the electron mean free path at $T = 300$ K, $\lambda = 50$ nm, the reflection coefficient for

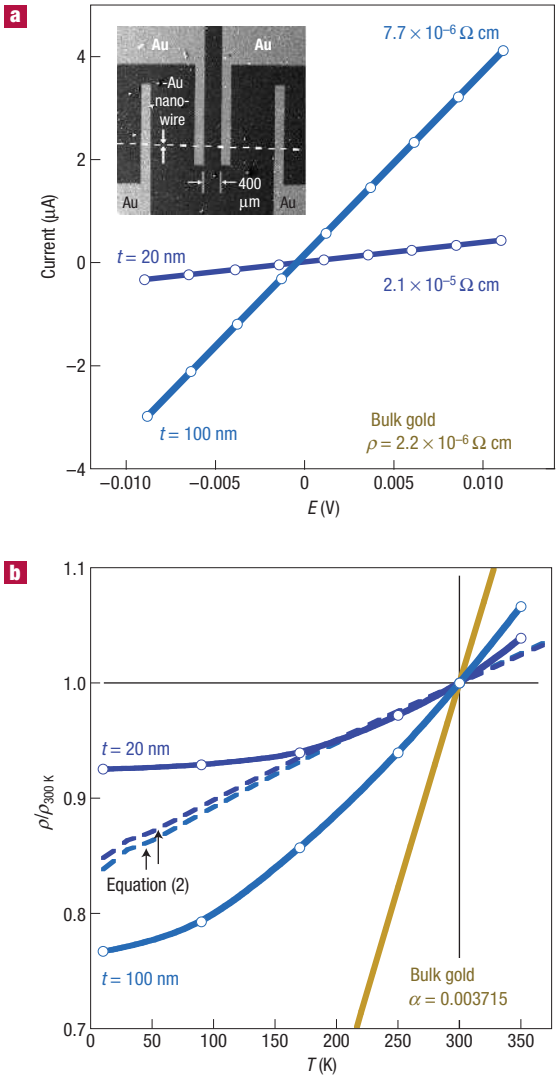

Figure 6 A high degree of wire uniformity results in nanowires that are electrically continuous for up to 1.0 cm. a, Current-versus-voltage curves acquired using four evaporated electrodes (inset). Data for two gold nanowires prepared by LPNE are shown. These nanowires had dimensions of 20 nm (thickness) × 233 nm (width), and 100 nm (thickness) × 166 nm (width)—the isolated wire length in both cases was 400 μm. **b**, Temperature dependence of the wire resistivity, ρ, normalized to the resistivity at 300 K, ρ_{300}, from 10 to 350 K, for the same two nanowires as shown in **a**. We also plot the resistivity of bulk gold and the temperature-dependent resistivities (dashed lines) calculated using equations (2) and (3), using the parameters indicated in the text. In this calculation, we took the temperature dependence of the electron mean free path to be inversely proportional to the resistivity for bulk gold.

grain boundaries, $R = 0.9$, and the fraction of electrons incident on wire surfaces that are specularly scattered, $p = 0.5$. We can predict the temperature-dependent ρ_0 in equation (2) using the Bloch–Grüneisen equation:

$$\rho(T) = C\frac{T^5}{\Theta^6}\int_0^{\Theta/T}\frac{x^5 dx}{(e^x - 1)(1 - e^{-x})} \qquad (3)$$

where the Debye temperature for gold, Θ, is 225 K (refs 16,24,25).

How well do these equations model the measured resistivity of our LPNE gold nanowires? Focusing first on the resistivity data at 300 K (Table 1), equation (2) predicts a resistivity that is too high for both nanowires when a grain boundary diameter of 20 nm is assumed. This disparity is actually larger, approximately one order of magnitude, for the larger of the two nanowires, suggesting that the assumed R value of 0.9 is too high[23]. A second discrepancy with equation (3) involves the temperature dependence of ρ: equation (3) predicts a nearly linear ρ versus T behaviour, whereas we see significant curvature to higher ρ values with diminishing temperature for both nanowires (Fig. 6b). We cannot explain this effect within the context of equations (2) and (3).

Two additional contributing factors to the resistivity are impurities in the electrodeposited gold, and a mismatch in the coefficients of thermal expansion for gold ($\kappa = 14 \times 10^{-6}\,K^{-1}$, 300 K) and the soda-lime glass support ($\kappa = 9 \times 10^{-6}\,K^{-1}$, 300 K). This mismatch, which increases with decreasing temperature, means that the length of the gold nanowire shrinks more rapidly with decreasing temperature than the glass surface on which it is supported, placing it in tension. The total strain that accumulates in cooling from 300 to 80 K, for example, is significant: approximately 0.7 μm for the 400 μm nanowires investigated here. Investigations of nanowires on surfaces having different κ values will be necessary to determine the influence of this effect on the wire resistivity.

Table 1 Experimentally measured resistivities at 300 K, $\rho_{300\,K}$, for two gold nanowires, and a comparison with calculated resistivities and bulk gold.

Wire thickness (nm)	Wire width (nm)	Grain diameter (nm)	$\rho_{300\,K}$ (Ω cm)
	Experimental		
20	233	10–20*	2.05×10^{-5}
100	166	10–20*	7.78×10^{-6}
	Calculated†		
20	233	100	1.87×10^{-5}
20	233	20	7.73×10^{-5}
100	166	100	1.77×10^{-5}
100	166	20	7.62×10^{-5}
	Bulk gold		
			2.20×10^{-6}

* Estimated from scanning electron micrographs.

† Calculated using equations (2) and (3).

METHODS

We implemented the seven-step LPNE procedure shown in Fig. 1 as follows. We cleaned soda-lime glass microscope slides in aqueous Nochromix solution, air dried them and diced them into 1″ × 1″ squares. Onto each square, we deposited a nickel film (ESPI, 5N purity), 20–100 nm in thickness, by hot-filament evaporation at a rate of 0.5–1.5 Å s^{-1} (step 1). We monitored the film thickness and evaporation rate using a quartz-crystal microbalance (Sigma Instruments).

We then coated nickel-covered glass squares with a positive photoresist layer (Shipley 1808) by spin coating (step 2). This involved the deposition of a 1 ml aliquot of photoresist onto each square and the rotation of the square at 2,500 r.p.m. for 40 s. This produced a photoresist thickness (after soft baking) of ~1 μm. We soft-baked freshly coated squares at 90 °C for 30 min. After cooling to room temperature, we pressed a transparent contact mask onto the photoresist with a quartz plate and exposed this masked surface to a hand-held ultraviolet lamp, with a wavelength of ≈365 nm and an output power of 0.5 mW cm^2 for 2 min. We then soaked the slide first in a developer–water solution (one part Shipley MF-351 to four parts water) for 20 s, and then in pure water for 1 min, before drying in a stream of ultra-high-purity (UHP) N_2

(step 3). We then electrochemically removed exposed nickel (step 4) and electrodeposited palladium, platinum or gold (step 5) onto the nickel nanoband electrodes produced by this process.

We carried out the electrochemical stripping of the nickel and the electrodeposition of these metals in a 50 ml, one-compartment, three-electrode cell. We carried out nickel dissolution in aqueous 0.1 M KCl containing 0.1 ml of concentrated HCl. We electroplated palladium from an aqueous solution containing 2 mM $PdCl_2$ and 0.1 M KCl at 0.225 V versus SCE. We electroplated platinum from a solution containing 0.1 M KCl and 1.0 mM K_2PtCl_6 at 0.025 V versus SCE. We electroplated gold from aqueous commercial gold-plating solution (Clean Earth Solutions—a 6 mM $AuCl_3$ solution), with added 1.0 M KCl at −0.90 V versus SCE. We prepared all aqueous solutions using Millipore MilliQ water ($\rho > 18.0\,M\Omega$ cm). We also used an SCE and a 2 cm^2 Pt foil counter-electrode. We carried out both the stripping and deposition on a computer-controlled EG&G 273A potentiostat/galvanostat.

We achieved nickel stripping by securing the photoresist-covered nickel film with self-closing metal tweezers, and placing part of the exposed nickel film in the nickel-stripping solution. We then held the film at a potential of −0.085 V versus SCE for 1,000 s. This removed all of the exposed nickel and produced an 'undercut' beneath the photoresist at each nickel edge produced by photolithography on the surface. We then rinsed the slide with Nanopure water, and placed it in the palladium-deposition solution. We electrodeposited palladium metal by holding the nickel film at a potential of +0.225 V versus SCE for times ranging from 25 to 400 s. We then rinsed the glass slide with Nanopure water and dried it with UHP N_2. We then removed the photoresist (step 6) by rinsing the slide with electronic grade acetone (Acros), methanol (Fisher) and Nanopure water, respectively, before drying with UHP N_2. We then removed the excess nickel film by washing with dilute HNO_3 (step 7). Complete removal of nickel required exposure to 5–7 M HNO_3 for at least 8 h.

We acquired SEM images using a Philips model XL-30FEG operating at 10 kV. We sputter coated a thin gold film onto the glass slides before imaging to prevent charging in the SEM. We obtained atomic force microscopy images on a Park Scientific Instruments model CP atomic force microscope. We collected the 256 pixels × 256 pixels images in non-contact mode, using Mikromasch AFM tips with a scan rate of 0.5 lines s^{-1}. After collection, we flattened images using a line-by-line second-order fit to remove any curvature imparted by the piezoelectric scanning tube.

Received 14 July 2006; accepted 6 September 2006; published 22 October 2006.

References

1. Spicer, D. F., Rodger, A. C. & Varnell, G. L. Computer-controlled pattern generating system for use with electron-beam writing instruments. *J. Vac. Sci. Technol.* **10,** 1052–1055 (1973).
2. Varnell, G. L., Spicer, D. F. & Rodger, A. C. E-Beam writing techniques for semiconductor-device fabrication. *J. Vac. Sci. Technol.* **10,** 1048–1051 (1973).
3. Vieu, C. *et al.* Electron beam lithography: Resolution limits and applications. *Appl. Surf. Sci.* **164,** 111–117 (2000).
4. Berger, S. D. & Gibson, J. M. New approach to projection-electron lithography with demonstrated 0.1 μM linewidth. *Appl. Phys. Lett.* **57,** 153–155 (1990).
5. Berger, S. D. *et al.* Projection electron-beam lithography—A new approach. *J. Vac. Sci. Technol. B* **9,** 2996–2999 (1991).
6. Liddle, J. A. *et al.* Space-charge effects in projection electron-beam lithography: Results from the SCALPEL proof-of-lithography system. *J. Vac. Sci. Technol. B* **19,** 476–481 (2001).
7. Jorritsma, J., Gijs, M. A. M., Kerkhof, J. M. & Stienen, J. G. H. General technique for fabricating large arrays of nanowires. *Nanotechnology* **7,** 263–265 (1996).
8. Natelson, D., Willett, R. L., West, K. W. & Pfeiffer, L. N. Fabrication of extremely narrow metal wires. *Appl. Phys. Lett.* **77,** 1991–1993 (2000).
9. Natelson, D., Willett, R. L., West, K. W. & Pfeiffer, L. N. Geometry-dependent dephasing in small metallic wires. *Phys. Rev. Lett.* **86,** 1821–1824 (2001).
10. Melosh, N. A. *et al.* Ultrahigh-density nanowire lattices and circuits. *Science* **300,** 112–115 (2003).
11. Thompson, M. A., Menke, E. J., Martens, C. C. & Penner, R. M. Shrinking nanowires by kinetically controlled electrooxidation. *J. Phys. Chem. B* **110,** 36–41 (2006).
12. Nagale, M. P. & Fritsch, I. Individually addressable, submicrometer band electrode arrays. 1. Fabrication from multilayered materials. *Anal. Chem.* **70,** 2902–2907 (1998).
13. Bard, A. J. *Electrochemical Methods: Fundamentals and Applications* (Wiley, New York, 2001).
14. Walter, E. C. *et al.* Noble and coinage metal nanowires by electrochemical step edge decoration. *J. Phys. Chem. B* **106,** 11407–11411 (2002).
15. Durkan, C. & Welland, M. E. Size effects in the electrical resistivity of polycrystalline nanowires. *Phys. Rev. B* **61,** 14215–14218 (2000).
16. Marzi, G. D., Iacopino, D., Quinn, A. J. & Redmond, G. Probing intrinsic transport properties of single metal nanowires: Direct-write contact formation using a focused ion beam. *J. Appl. Phys.* **96,** 3458–3462 (2004).
17. Yang, F. Y. *et al.* Large magnetoresistance of electrodeposited single-crystal bismuth thin films. *Science* **284,** 1335–1337 (1999).
18. Yang, F. Y. *et al.* Large magnetoresistance and finite-size effect in electrodeposited bismuth lines. *J. Appl. Phys.* **89,** 7206–7208 (2001).
19. Chiu, P. & Shih, I. A study of the size effect on the temperature-dependent resistivity of bismuth nanowires with rectangular cross-sections. *Nanotechnology* **15,** 1489–1492 (2004).
20. Fuchs, K. The conductivity of thin metallic films according to the electron theory of metals. *Proc. Camb. Phil. Soc.* **34,** 100–108 (1938).
21. Sondheimer, E. H. The mean free path of electrons in metals. *Adv. Phys.* **1,** 1–42 (1952).
22. Mayadas, A. F. & Shatzkes, M. Electrical-resistivity model for polycrystalline films—case of arbitrary reflection at external surfaces. *Phys. Rev. B* **1,** 1382–1389 (1970).
23. Steinhogl, W., Schindler, G., Steinlesberger, G., Traving, M. & Engelhardt, M. Comprehensive study of the resistivity of copper wires with lateral dimensions of 100 nm and smaller. *J. Appl. Phys.* **97,** 023706 (2005).
24. Marom, H. & Eizenberg, M. The temperature dependence of resistivity in thin metal films. *J. Appl. Phys.* **96,** 3319–3323 (2004).
25. Steinhogl, W., Schindler, G., Steinlesberger, G. & Engelhardt, M. Size-dependent resistivity of metallic wires in the mesoscopic range. *Phys. Rev. B* **66,** 075414 (2002).

Acknowledgements

The National Science Foundation funded this work through grant CHE-0111-557.
Correspondence and requests for materials should be addressed to R.M.P.

Competing financial interests

The authors declare that they have no competing financial interests.